AGU PUBLICATIONS

JGR

Journal of Geophysical Research: Solid Earth

RESEARCH ARTICLE
10.1002/2016JB013064

Key Points:
- Slab tear in southern Peru north of the Nazca Ridge created new mantle pathway
- Pronounced low-velocity anomaly is detected beneath the flat slab
- Slab anisotropy reflects substantial along strike variations in the slab's internal deformation

Supporting Information:
- Supporting Information S1
- Table S1

Correspondence to:
S. Antonijevic,
sanjaknezevicantonijevic@gmail.com

Citation:
Antonijevic, S., L. S. Wagner, S. L. Beck, M. D. Long, G. Zandt, and H. Tavera (2016), Effects of change in slab geometry on the mantle flow and slab fabric in Southern Peru, *J. Geophys. Res. Solid Earth*, *121*, 7252–7270, doi:10.1002/2016JB013064.

Received 6 APR 2016
Accepted 18 SEP 2016
Accepted article online 21 SEP 2016
Published online 9 OCT 2016

Effects of change in slab geometry on the mantle flow and slab fabric in Southern Peru

Sanja Knezevic Antonijevic[1], Lara S. Wagner[2], Susan L. Beck[3], Maureen D. Long[4], George Zandt[3], and Hernando Tavera[5]

[1]Department of Geological Sciences, University of North Carolina at Chapel Hill, Chapel Hill, North Carolina, USA, [2]Department of Terrestrial Magnetism, Carnegie Institution for Science, Washington, District of Columbia, USA, [3]Department of Geosciences, University of Arizona, Tucson, Arizona, USA, [4]Department of Geology and Geophysics, Yale University, New Haven, Connecticut, USA, [5]Instituto Geofísico del Perú, Lima, Perú

Abstract The effects of complex slab geometries on the surrounding mantle flow field are still poorly understood. Here we combine shear wave velocity structure with Rayleigh wave phase anisotropy to examine these effects in southern Peru, where the slab changes its geometry from steep to flat. To the south, where the slab subducts steeply, we find trench-parallel anisotropy beneath the active volcanic arc that we attribute to the mantle wedge and/or upper portions of the subducting plate. Farther north, beneath the easternmost corner of the flat slab, we observe a pronounced low-velocity anomaly. This anomaly is caused either by the presence of volatiles and/or flux melting that could result from southward directed, volatile-rich subslab mantle flow or by increased temperature and/or decompression melting due to small-scale vertical flow. We also find evidence for mantle flow through the tear north of the subducting Nazca Ridge. Finally, we observe anisotropy patterns associated with the fast velocity anomalies that reveal along strike variations in the slab's internal deformation. The change in slab geometry from steep to flat contorts the subducting plate south of the Nazca Ridge causing an alteration of the slab petrofabric. In contrast, the torn slab to the north still preserves the primary (fossilized) petrofabric first established shortly after plate formation.

1. Introduction

The subduction zone in southern Peru is characterized by the complex geometry of the descending oceanic Nazca Plate that changes from steep to flat at ~16°S [*Cahill and Isacks*, 1992]. Along the flat slab segment, the ~40–45 Ma old Nazca plate [*Müller et al*., 2008] starts to subduct at a normal dip angle to ~90 km depth. It then bends and continues almost horizontally for several hundred kilometers beneath the South American continent (Figure 1).

Earlier studies recognized the spatial correlation between the flat slab and the subducting Nazca Ridge [*Gutscher et al*., 2000]. The ridge was formed as a hot spot track either of the Easter plume, while the plume was still sufficiently close to the East Pacific Rise [*Steinberger*, 2002], or near Salas y Gomez, ~400 km farther east [*Ray et al*., 2012]. The oceanic crust of the ridge is considerably thickened with a ~5 km thick basaltic oceanic crust above an ~12 km thick gabbroic layer [*Hampel et al*., 2004; *Couch and Whitsett*, 1981; *Macharé and Ortlieb*, 1992]. Due to the oblique orientation of the ridge with respect to the convergence direction [*DeMets et al*., 2010] (Figure 1), the ridge was located significantly farther north (at ~11.2°S) when it started to subduct ~11 Ma [*Hampel*, 2002; *Rosenbaum et al*., 2005]. While the combination of several factors such as trench retreat, suction, and ridge subduction acted together to form the flat slab, the removal of the ridge, as it moved too far south over time, caused the flat slab to fail to the north [*Antonijevic et al*., 2015] (Figure 1). In contrast, along the southern edge of the flat slab the descending plate is still continuous but sharply contorted [*Dougherty and Clayton*, 2014; *Phillips and Clayton*, 2014; *Ma and Clayton*, 2014].

Seismic anisotropy is often used to better understand current and/or past deformation patterns within the mantle [*Long and Becker*, 2010]. Typically, the crystallographic preferred orientation (CPO) of olivine is invoked to explain the seismic anisotropy within the upper mantle. Constraints from laboratory experiments and natural samples have led to the development of simple rules of thumb for relating seismic anisotropy directions to mantle flow directions [*Karato et al*., 2008]. These simplified relationships are useful in developing general interpretations of seismic anisotropy data; however, they obscure potential complications due to mantle flow fields that vary in space and time, as well as the complexities of CPO development, particularly

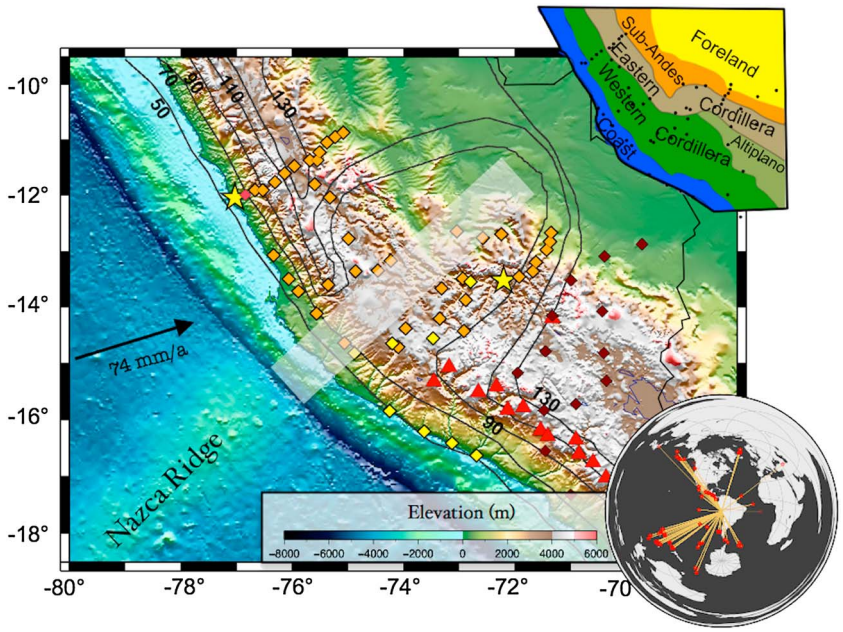

Figure 1. Reference map of the Peruvian flat slab region. Diamonds are stations used in this study: orange—PULSE, dark red—CAUGHT, yellow—PERUSE, and light red—permanent NNA station. Yellow stars represent cities Lima (left) and Cusco (right). Contour lines (in km) refer to subducting plate [*Antonijevic et al.*, 2015]. Red triangles are Holocene volcanoes (Instituto Geológico Minero y Metalúrgico – INGEMMET, On-line Catalog accessed at http://www.ingemmet.gob.pe, Peru, 2014). The black arrow denotes relative motion of the Nazca Plate [*Gripp and Gordon*, 2002]. The shaded area indicates projection of subducted Nazca Ridge. Insert 1: major morphostructural units [*Jaillard et al.*, 2000] with stations used in the study (black dots). Insert 2: teleseismic events used in the study.

in settings such as a subduction zone [e.g., *Skemer et al.*, 2012; *Faccenda and Capitanio*, 2013; *Di Leo et al.*, 2014; *Skemer and Hansen*, 2015].

Based on SKS splitting, *Russo and Silver* [1994] reported trench-parallel fast directions along the Central Andean subduction zone. Their explanation for this anisotropic pattern is the formation of CPO of olivine due to trench-parallel mantle flow beneath the subducting slab, which in turn is induced by trench rollback. Recent shear wave splitting studies, however, have found more complex patterns across southern Peru. Results of local shear wave splitting reveal predominantly trench-parallel alignments of fast directions north of the subducting ridge and heterogeneous anisotropic patterns south of the ridge [*Eakin et al.*, 2014]. Shear wave splitting analyses of SKS, sSKS, and PKS phases between 10° and 18°S illuminate distinct spatial variations along strike, where the projected subducting Nazca Ridge again marks a sharp boundary in the anisotropic patterns [*Eakin et al.*, 2015]. Multilayered anisotropy characterized by subslab trench-normal and supraslab trench-parallel fast directions has been reported north of the ridge [*Eakin and Long*, 2013], while the ridge track is associated with generally little or no splitting of SKS phases [*Eakin et al.*, 2015].

Complex patterns of seismic anisotropy have been observed in other subduction zones worldwide. Often, these are associated with unusual slab geometry. Examples include the narrow flat slab in central Chile/Argentina [*Anderson et al.*, 2004], the torn slab in northern Colombia [*Porritt et al.*, 2014], and the slab edge present in Kamchatka [*Peyton et al.*, 2001]. The complexity of these various tectonic settings demonstrates the need for 3-D constraints on mantle flow and slab dynamics in these areas. Here we combine Rayleigh wave anisotropy with 3-D shear wave velocity structure to investigate mantle flow and slab fabric in southern Peru. Unlike shear wave splitting, Rayleigh waves at different periods provide constraints on the depth of the observed anisotropy that are otherwise difficult to attain. We find that slab tear north of the projected Nazca Ridge creates a new pathway for mantle flow between the region above the recently torn slab to the north and area below the flat slab to the south. This lateral mantle flow may contribute to the low shear wave velocities we observe beneath the inboard easternmost corner of the flat slab. We find evidence for modified slab fabric along the southern edge of the flat slab, consistent with previous results and interpretations of *Eakin et al.* [2016], but preserved fossil spreading fabric within the torn slab to the north. The contrast in slab fabric

along the strike supports the hypothesis that the extension due to change in slab geometry from steep to flat may alter the internal slab anisotropy upon subduction.

2. Data

Data were collected from several seismic networks: PULSE (Peru Lithosphere and Slab Experiment), CAUGHT (Central Andean Uplift and Geodynamics of High Topography), PERUSE (Peru Subduction Experiment), and the Global Seismic Network permanent stations in Lima, Peru (Figure 1). The PULSE seismic network was part of a 2 year (2011–2013) project consisting of 40 three-component broadband seismometers, sampling at 40 samples/s, installed along three transects in central and southern Peru. The northern transect extended between Lima and Satipo with ~18 km station intervals. The middle transect extended from Pisco to Ayacucho with interstation distances varying from ~25 km to ~60 km. The southern transect stretched from the coast to the Amazon Basin, with station intervals of ~40 km from the coast to Cusco and ~15 km from Cusco toward the Basin. The data set is augmented with records from 12 adjacent CAUGHT stations [*Ward et al*., 2013] and eight PERUSE stations [*Phillips et al*., 2012] that improved our resolution along the southern edge of the flat slab.

We used teleseismic events with magnitudes greater than 6.2 that occurred during the PULSE deployment between 25° and 125° from the center of the array. Most of these events come from the SW direction (from the Kermadec-Tonga subduction zone) and NNW (from the Alaska subduction zone). To ensure a more heterogeneous back-azimuthal coverage, we limited events from oversampled back azimuths and added smaller but well recorded events ($M < 6.2$) coming from less represented directions (Figure 1, insert 2). We also included well-recorded earthquakes with magnitudes greater than 8 and epicentral distances beyond 125° from the center of the array.

Instrument responses were normalized and traces were bandpassed using a Butterworth filter, 7–10 mHz wide, centered on the frequency of interest. The fundamental mode Rayleigh wave was windowed for 12 periods in the band between 0.007 and 0.03 Hz and cut with a 50 s cosine taper at either end. The width of the window varied with different events and periods, but for particular period and event it was held constant. Phases and amplitudes of waves for each period at each station were later determined using Fourier analysis.

3. Methods

We invert for Rayleigh wave phase velocities and then use the obtained 2-D phase velocities to determine isotropic 3-D shear velocity structure. We use the finite-frequency two-plane wave method developed by *Forsyth and Li* [2005] and *Yang and Forsyth* [2006] to invert for Rayleigh wave phase velocities and anisotropy. Phase velocities are approximated by

$$C(\omega,\theta) = B_0(\omega) + B_1(\omega)\cos(2\theta) + B_2(\omega)\sin(2\theta),$$

where C is phase velocity at a specific frequency (ω) and azimuth (θ), leaving out the higher order terms [*Smith and Dahlen*, 1973; *Weeraratne et al*., 2007]. The fast propagation direction is calculated as 0.5*arctan (B_2/B_1), while the peak-to-peak anisotropy magnitude is represented as $2 \times (B_1{}^2 + B_2{}^2)^{½}$.

Grid nodes are approximately equidistant and are generated as a function of azimuth and distance from a pole of rotation, located 90° North of the center of the array (see *Forsyth and Li* [2005] for further details). We use 0.33° grid node spacing for isotropic and 0.66° for anisotropic terms. Starting Rayleigh wave phase velocities are important for a stable inversion. We calculate the 2-D starting phase velocities across the study area using the velocity model of *James* [1971] for the crust and the IASPEI91 for the mantle [*Kennett and Engdahl*, 1991] and predict phase velocities applying the forward algorithm of *Saito* [1988]. The crustal thickness is highly variable in our study area, ranging from thin oceanic crust to ~70 km thick crust below the high Andean peaks. Thus, we create a 2-D crustal thickness map using results from *Tassara et al*. [2006], smoothed along the coast, and adjust the starting model accordingly at each grid point in the inversion (supporting information Figures S1 and S2).

The inversion is regularized with a combination of a priori model covariance, set to 0.15 km/s for isotropic velocities and 0.05 km/s for anisotropic terms. The choice of regularization parameters is always a trade-off between the amplitude of the model corrections and data misfit. We tested values for isotropic velocities

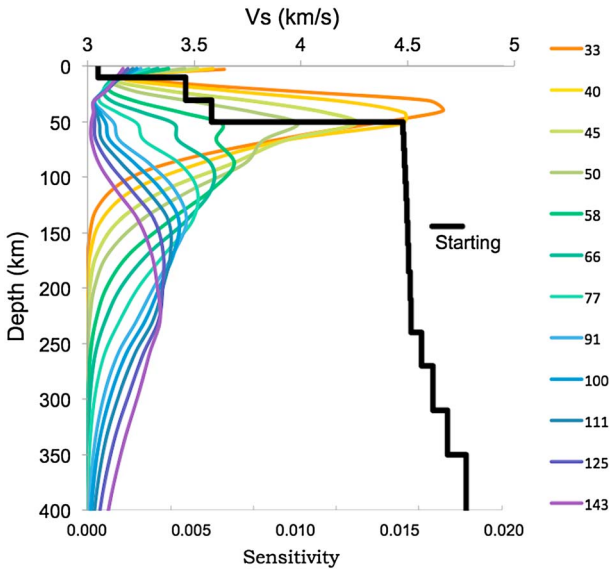

Figure 2. Sensitivity kernels for periods used in the study with 1-D starting shear wave velocity model.

ranging from 0.05 km/s to 0.5 km/s. Smaller values result in overdamped inversions that reveal prominent features required by the data but underestimate their amplitudes. Larger values result in underdamped inversions that produce spurious features with unreasonably large and rapidly varying amplitudes. To ensure a stable solution, we also check the misfit between predicted and observed phase velocities in the shear wave inversion. Finally, we choose 0.15 km/s for isotropic velocities, since the average root-mean-square (RMS) phase misfit between predicted and observed phase velocities in the shear wave inversion increases rapidly at model covariance greater than this value (supporting information Figure S3).

Rayleigh wave phase velocities are sensitive to shear wave velocity structure (Figure 2). We invert the obtained Rayleigh wave phase velocities for shear wave velocities using the algorithm of *Saito* [1988] and *Weeraratne et al.* [2003] (supporting information Figure S2). The starting model is the same as the one used to predict phase velocities (Figure 2). The vertical resolution is controlled by the sensitivities of the periods used in the study to the shear wave velocity structure with depth (Figure 2). It is also affected by the thickness of layers, so we parameterize our shear wave velocity columns such that the diagonal value in the resolution matrix for a particular layer ranges between 0.1 and 0.3. Our vertical resolution drops below 0.1 at depths shallower than ~40 km and greater than ~200–250 km (supporting information Figure S4).

4. Results

4.1. Shear Wave Velocity Model

The main differences between our new shear wave velocity model and the model presented by *Antonijevic et al.* [2015] include improved azimuthal distribution of the teleseismic events used in the study and taking into account anisotropy in the phase velocity maps, which may change the isotropic solution. However, our results reveal very similar structures as previously reported by *Antonijevic et al.* [2015] (Figure 3 and supporting information Figure S5). North of the projected subducted Nazca Ridge we observe a dipping high velocity anomaly that coincides with the location of a scatterer identified in earlier studies of ScSp phases [*Snoke et al.*, 1979] (Figure 3d). The dipping high shear wave velocities are overlain by a dipping low-velocity anomaly. The low-velocity anomaly is located beneath an unusually high heat flow measurement (196 mW/m^2) [*Uyeda et al.*, 1980]. The structures are consistent with a previously proposed slab tear and the warm asthenospheric corner flow above the now normally dipping slab to the west [*Antonijevic et al.*, 2015] (Figures 3a–3d).

Along the projected Nazca Ridge we observe an increase in shear wave velocities from ~4.4 km/s near the trench to >4.55 km/s ~100–~ 150 km away from the trench, where the plane of seismicity roughly illuminates the top of the slab (Figure 3e). However, the observed high velocities continue much further inboard than the plane of seismicity and start to dip ~600–~ 680 km away from the trench. The feature is consistent with the previously proposed flat slab that resumes steep subduction far to the east [*Antonijevic et al.*, 2015]. Below the observed high velocities, beneath the southeastern corner of the flat slab, we observe a pronounced low-velocity anomaly. At long periods (77–111 s) we observe prominent low velocities centered at ~72.5°W ~13°S, with the greatest phase velocity reduction (~5%) at 91 s (Figure 4). In the shear wave velocity model, the low velocities first appear at ~125 km depth. Velocities decrease with increasing depth up to ~145 km where *Vs* approaches 4.2 km/s (Figures 3c and 3e and supporting information Figure S5). By ~165 km depth

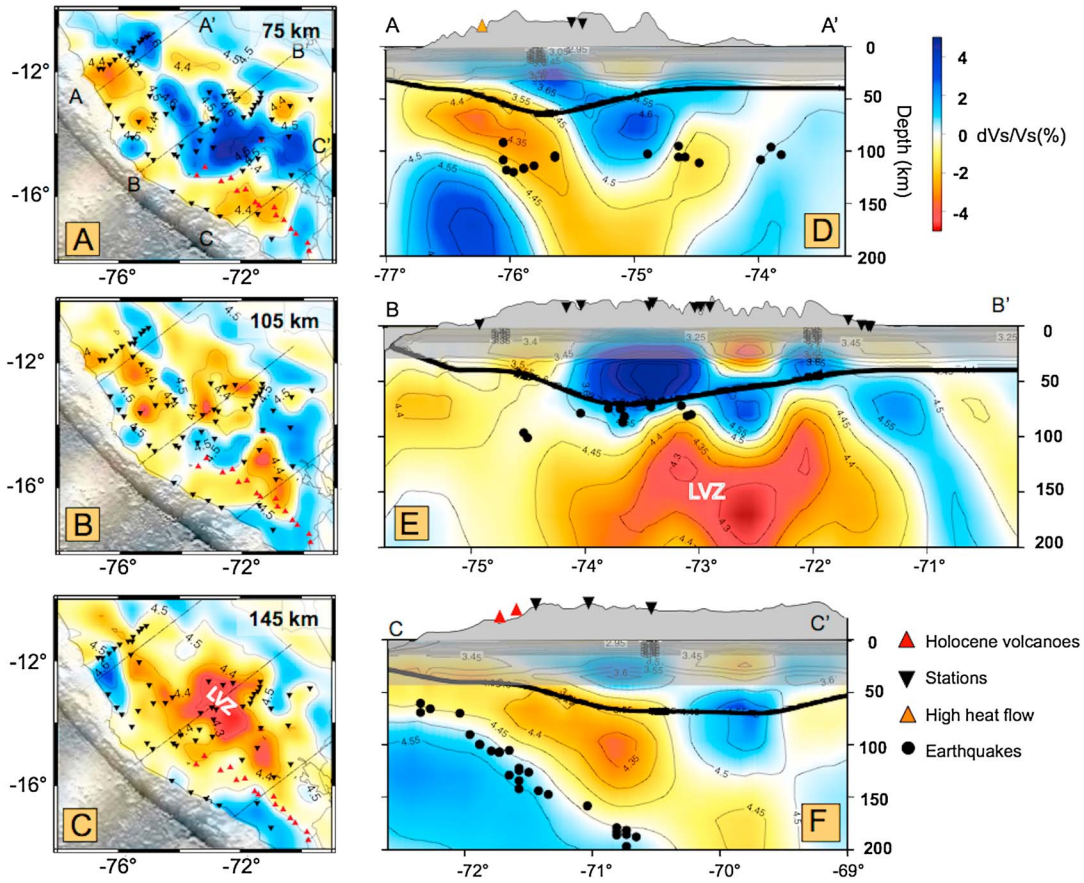

Figure 3. Shear wave velocity maps at (a) 75, (b) 105, and (c) 145 km depth and (d) profiles along the slab tear observed to the north, (e) flat slab along the subducting Nazca Ridge, and (f) steeply subducting slab to the south. Colors represent velocity deviations with respect to the reference model (Figure 2), while contours show absolute velocities. Black dots show earthquake locations (from *Antonijevic et al.* [2015]), black inverted triangles are stations, red triangles are Holocene volcanoes, and the orange triangle (Figure 3d) represents the location of an unusually high heat flow measurement [*Uyeda et al.*, 1980]. LVZ refers to low-velocity anomaly discussed in the text.

the anomaly shifts east and becomes less pronounced; by ~200 km depth velocities increase above 4.4 km/s, but our resolution starts to decrease (supporting information Figure S4). This feature is consistent with the observations of *Scire et al.* [2016], who also found significant velocity reductions under the easternmost corner beneath the Peruvian of the flat slab using finite frequency teleseismic *P* and *S* wave tomography. The anomaly is more pronounced in their shear wave velocity model, with the greatest velocity reduction (almost ~9%) between ~130 and ~200 km depth. The anomaly is still visible up to ~500 km depth but with less pronounced velocity reduction. The observed low-velocity anomaly is also consistent with a recent receiver function study using results from the dense line of seismic stations deployed along the Nazca Ridge track [*Ma and Clayton*, 2015]. The anomaly is substantially more pronounced with plotted events from the SE than with the events plotted from the NW, indicating significant along strike variations in the structure.

To the south, we observe a progressive change in the dip of the slab from flat to steep. Our observations are consistent with a continuously contorted slab as reported in previous studies [*Dougherty and Clayton*, 2014; *Phillips and Clayton*, 2014; *Ma and Clayton*, 2014]. At ~17°S we observe high shear wave velocities aligned with the 30° dipping plane of seismicity (Figure 3f). Above the high velocities we observe a low-velocity anomaly, roughly located beneath the active volcanic arc, consistent with the presence of asthenospheric corner flow.

4.2. Azimuthal Anisotropy

North of the projected subducted Nazca Ridge at short periods (33 s, 40 s), we observe a trench-parallel alignment of fast directions with magnitudes up to 2.5% (dashed green area in Figure 4a and Suppl. figure 6a). These are colocated with low Rayleigh wave phase velocities. The alignment of fast directions is consistent

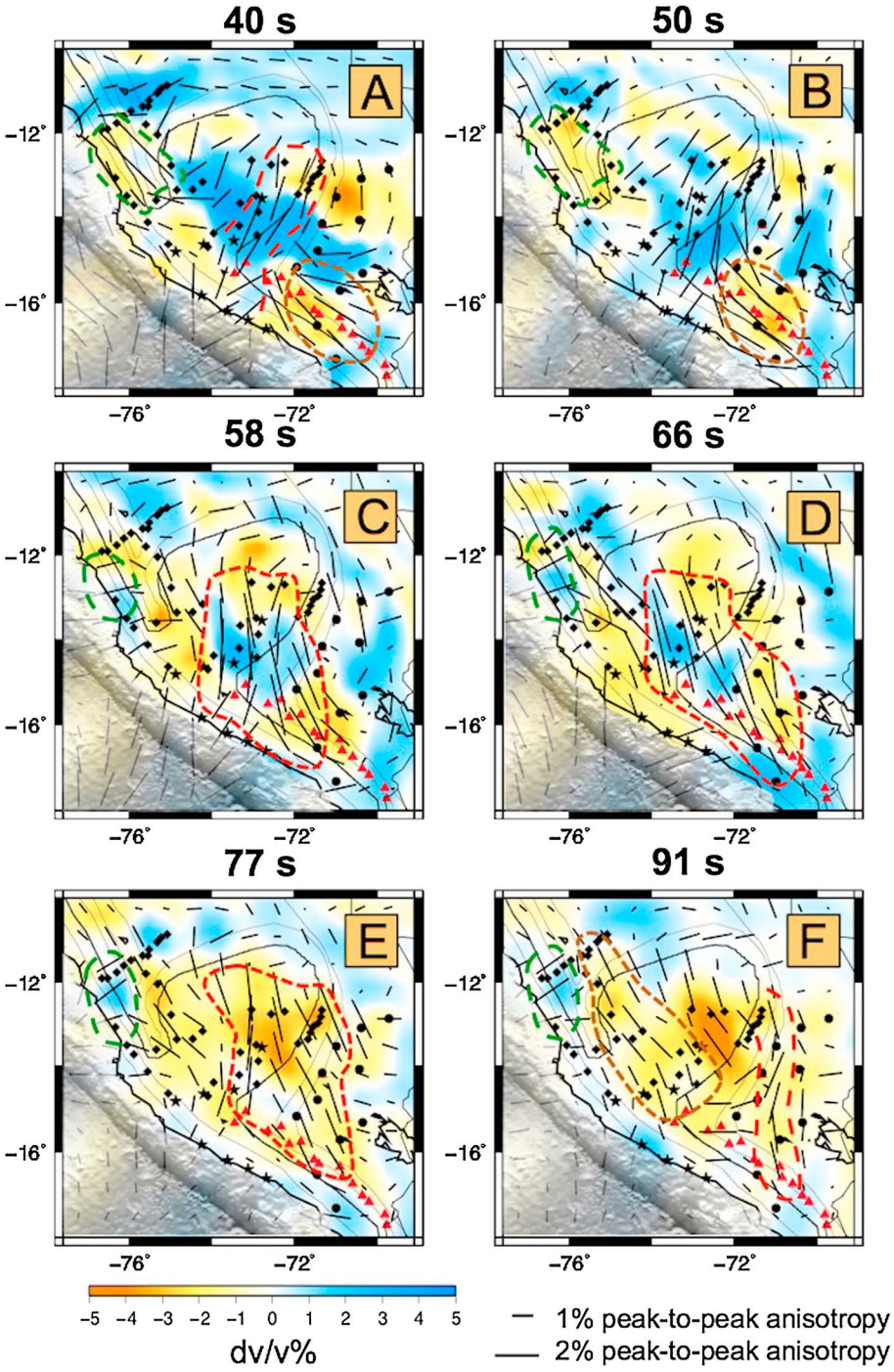

Figure 4. Rayleigh wave azimuthal anisotropy for periods 40, 50, 58, 66, 77, and 91 s. Black bars represent the fast directions scaled according to magnitude. Background colors are Rayleigh wave phase velocity deviations with respect to starting model (supporting information Figure S2). Red triangles represent Holocene volcanoes. Black rectangles, circles, and stars are stations used in the study. Contour lines represent the subducting plate with highlighted 90 km depth contour (from *Antonijevic et al.* [2015]). Dashed areas denote patterns discussed in the text.

with the results of local shear wave splitting [*Eakin et al.*, 2014]. At 50 s we observe little to no anisotropy in this area (Figure 4b, dashed green area). Along the coast near Lima and toward the Western Cordillera at intermediate and long periods (58 s - 125 s) we observe a trench-normal alignment of fast directions associated with fast Rayleigh wave phase velocities (dashed green area in Figures 4c–4f and supporting

information Figures S6c–S6e). The anisotropic feature occurs in the area where the torn slab has been earlier inferred [*Antonijevic et al*., 2015]. The sensitivity kernels of intermediate periods (Figure 2) help us to constrain the observed pattern to the depth of the torn slab (Figure 3d). Going toward the Eastern Cordillera and the Sub-Andean region (major morphostructural units are shown in Figure 1, insert 1), fast directions at intermediate and long periods become trench parallel and are collocated with low Rayleigh wave phase velocities (dashed brown area in Figure 4f and supporting information Figure S6c and Figures 4c–4e and supporting information Figures S6d–S6f). The difference in the observed patterns at short periods (trench parallel) (Figure 4a and supporting information Figure S6a, dashed green area) and long periods (trench normal) (Figures 4c–4f and supporting information Figures S6c–S6e, dashed green area) near the coast to the north of the Nazca Ridge indicates the presence of multilayered anisotropy, consistent with the shear wave splitting results of *Eakin and Long* [2013]. The dominant trench-parallel alignment of fast directions at long periods beneath the Eastern Cordillera (dashed brown area in Figure 4f and supporting information Figure S6c) is consistent with the SKS splitting results of *Russo and Silver* [1994] as well as the more recent results using SKS, sSKS, and PKS shear wave splitting of *Eakin et al*. [2015].

Along the southern end of the flat slab we observe a trench-perpendicular alignment of fast directions associated with high Rayleigh wave phase velocities at shorter periods (Figure 4a, dashed red area). The fast directions rotate to N-S at 45 and 50 s (Figure 4b and supporting information Figure S6b) and to NNW-SSE at intermediate periods (58 s, 66 s, 77 s, Figures 4c–4e) with anisotropic magnitudes up to 3%. At intermediate periods we note an interesting spatial distribution of the NNW-SSE oriented fast directions, which are closer to the coast at 58 s, and shift inboard at 66 s and 77 s (Figures 4c–4e, dashed red area). Based on the peak sensitivities of these periods (Figure 2), the observed pattern likely illuminates the subducting plate progressing to the northeast. At long periods (91–125 s) we observe a roughly N-S alignment of fast directions along ~71°W longitude, from ~16.5°S to ~12°S, which strikes parallel to the contours of the contorted slab at greater depths [*Kumar et al*., 2016; *Scire et al*., 2016] (dashed red area in Figure 4f and supporting information Figure S6c). Beneath the inboard easternmost corner of the flat slab, at ~72°W, ~13°S, we observe a trench-parallel alignment of fast directions at long periods (91 s, Figure 4f, 100 s, supporting information Figure S6c) with ~2% peak-to-peak anisotropy associated with pronounced low Rayleigh wave phase velocities. Long periods reveal a continuation of trench-parallel fast directions aligned with low Rayleigh wave phase velocities from the north toward the flat slab to the south, until ~15°S latitude where the fast directions start to rotate counterclockwise (dashed orange area in Figure 4f and supporting information Figure S6c).

To the south, where the slab descends steeply, we observe trench-parallel fast directions at periods between 40 and 50 s (dashed brown area in Figures 4a and 4b and supporting information Figure S6b). At longer periods (starting from 58 s) the fast directions here rotate NNW-SSE and shift inland, as noted above. The trench-parallel anisotropy aligns with the low velocities above the steeply subducting plate and is approximately located beneath the active volcanic arc (Figure 3f).

5. Resolution

The main new features observed in this study include a prominent low-velocity anomaly beneath the easternmost corner of the flat slab, fast directions collocated with fast anomalies, and trench-parallel anisotropy beneath the active arc to the south. We investigate the robustness of these features through a range of tests.

5.1. Low-Velocity Anomaly

The velocities observed beneath the eastern corner of the flat slab are unusually low but spatially constrained to one specific region. To demonstrate our ability to laterally resolve the observed low-velocity anomaly beneath the flat slab, we perform a series of checkerboard tests to test the size of the anomalies that can be recovered (Figure 5). We focus on long periods (77 s, 91 s, and 100 s) because these periods reveal significant phase velocity reductions (Figure 4). We also plot a 4.3 km/s contour line observed at 145 km depth, to indicate the locations of the observed low-velocity anomaly. The size of the anomaly is almost $2° \times 2°$, so in spite of the broad sensitivity kernels of long periods, the tests show that we do have sufficient spatial resolution to resolve an anomaly of this size.

To better understand our ability to resolve vertical extent and velocity reduction within the low-velocity anomaly, we perform forward modeling tests (Figure 6). We introduce low-velocity anomalies with 5%,

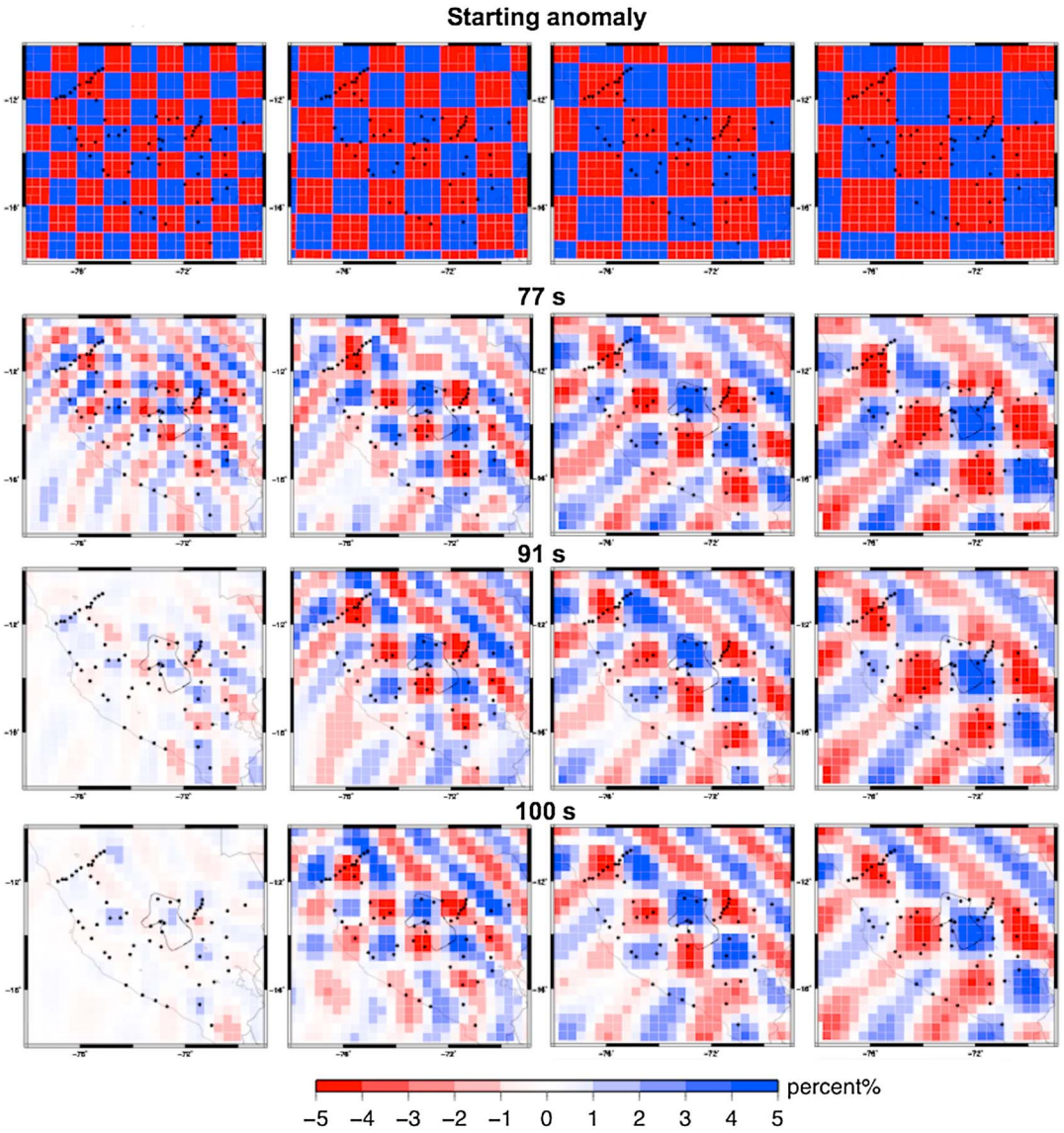

Figure 5. Checkerboard tests estimated from resolution matrix for 77, 91, and 100 s. Colors represent the recovered anomaly (see scale). Contour line of 4.3 km/s at 145 km (Figure 3c) is shown to denote the observed low-velocity anomaly. Dots are stations used in the study.

10%, 15%, 20%, 25%, 30%, and 35% shear wave velocity reduction and of various thicknesses and depths beneath the fast oceanic lithosphere lid, predict dispersion curves for these models, and compare the predicted with the observed phase velocities (Figure 6). We use the same regularization parameters and starting models as we use in the regular inversion to see how well we can recover the observed shear wave velocity anomaly. Generally, introduction of a thicker low-velocity anomaly results in greater velocity reduction. However, we were not able to match the observed phase velocity dispersion curves within error with any model that incorporates a shear wave velocity anomaly of 5% regardless of the vertical extent or depth of the anomaly. The models that do fit the observations within the confidence limits incorporate low velocities ranging from ~75 km thick anomalies with 10% velocity reduction to ~10 km thick anomalies with 35% velocity reduction. This test also shows that the actual low velocities within the observed shear wave velocity anomaly are probably underestimated.

5.2. Rayleigh Wave Azimuthal Anisotropy

The sum of the resolution matrix diagonals for anisotropic terms is shown in Figure 7 and supporting information Figures S7 and S8. The Western and Eastern Cordillera are the best resolved areas, while the resolution

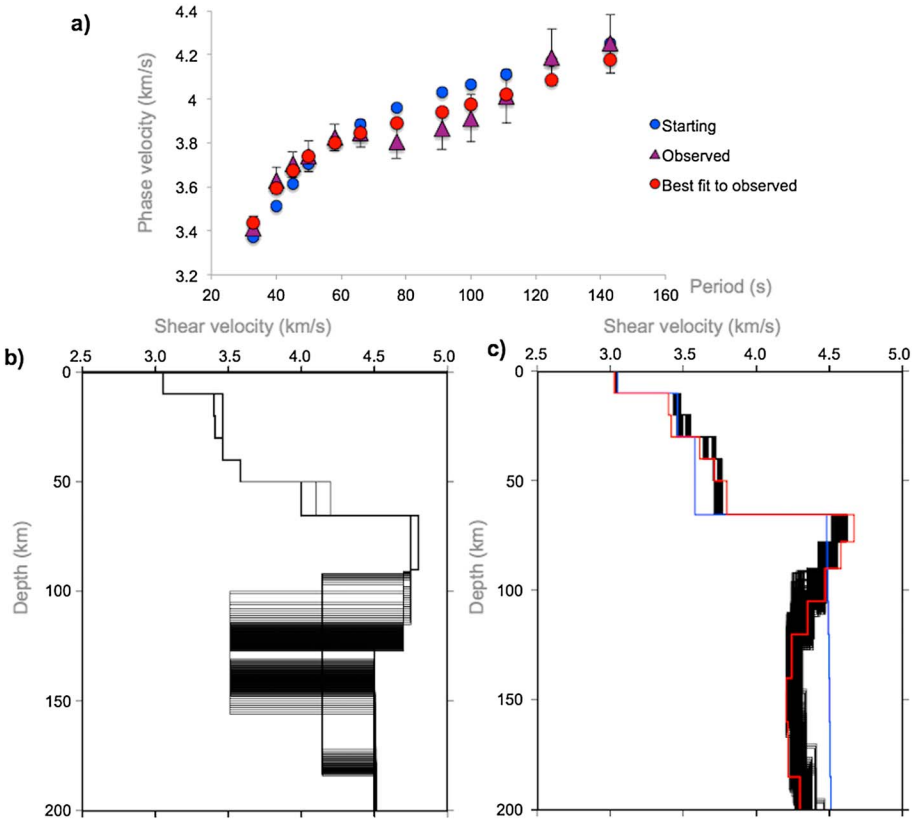

Figure 6. Recovery tests for the low-velocity anomaly beneath the flat slab. (a) Observed dispersion curve at 73.3°W, 13.8°S (purple triangles) with error bars representing one standard deviation of uncertainty. Blue dots represent the dispersion curve that corresponds to starting model shown with blue line in Figure 6c (see text for details). Red circles show the best fit to the observed dispersion curve yielding 1-D shear wave velocity model shown with red line in Figure 6c. (b) Suit of starting models with introduced low-velocity anomaly with velocity reduction ranging from 10% to 35% for which predicted dispersion curves fit the observations within the confidence limits. (c) Recovered models (black and gray lines) using predicted dispersion curves from 1-D shear wave velocity models shown in Figure 6b and our regular starting model (blue line). Red line represents the model obtained using the observed dispersion curve.

decreases toward the coast, Sub-Andes, and Foreland. The resolution also varies along strike, being the highest just south of the subducting Nazca Ridge, and between the ridge and dense northern line of seismic stations.

We performed a variety of tests to check the robustness of our results for Rayleigh wave phase anisotropy, including the sensitivity of our results to different a priori starting models and different damping parameters. We test the sensitivity of our results to the anisotropic characteristics of the starting model by using three different starting models: one with no anisotropy, one with uniform anisotropy of 2% strength with a N-S fast direction, and one with uniform anisotropy of 2% strength with an E-W fast direction (Figure 7 and supporting information Figures S7 and S8). These tests demonstrate the ability of the observations to constrain the patterns of fast directions, regardless of the starting model used. For example, north of the projected subducted Nazca Ridge, we observe a consistent trench-parallel alignment of fast directions at shorter periods near the coast and along Western Cordillera. At intermediate periods this pattern shifts inland and persists at long periods along the Eastern Cordillera, while areas near the coast appear to have roughly trench-perpendicular oriented fast directions. Also robust are the N-S to NNE-SSW oriented fast directions at intermediate periods along the flat slab segment. The N-S to NNE-SSW oriented fast directions along ~71°W longitude at long periods (91 s and 100 s) persist regardless of the starting model (Figure 7 and supporting information Figure S8). Finally, to the south, trench-parallel orientations of fast directions consistently appear at short periods (40–50 s) below the active volcanic arc where the slab subducts steeply (Figure 7 and supporting information Figure S7).

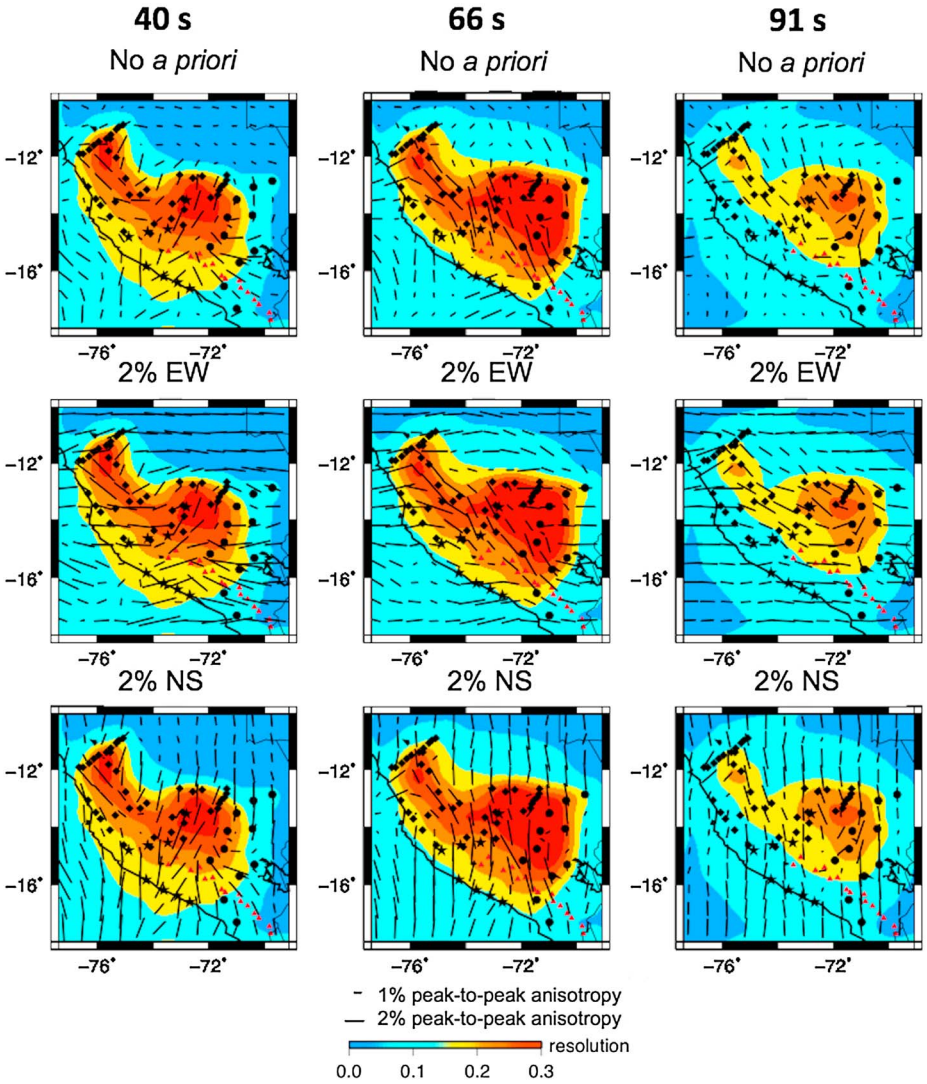

Figure 7. Resolution matrix diagonal for anisotropic terms and sensitivity test to different starting models for 40, 66, and 91 s. Black bars represent the fast directions scaled according to magnitude. (first row) Sensitivity to model with no a priori anisotropy, (middle row) to model with uniform anisotropy of 2% strength with an E-W fast direction, and (third row) to model with uniform anisotropy of 2% strength with a N-S fast direction. Background colors refer to resolution matrix diagonal. Red triangles are Holocene volcanoes. Black rectangles, circles, and stars are stations used in the study.

Tests using different damping parameters show that changing regularization parameters affects the anisotropic magnitude, but not the orientation of fast directions (supporting information Figure S9). In general, decreasing damping predictably increases magnitude. However, in well-resolved regions, a maximum magnitude is attained, regardless of further damping decrease. We use the highest damping (lowest covariance) that produces this maximum magnitude (covariance of 0.05) (supporting information Figure S9).

We estimate the standard errors for the strength and fast directions of our final model from the variation in B1 and B2 terms using an error propagation technique (supporting information Figure S10). Since the uncertainties related to change in regularization are much greater than the uncertainties in anisotropic strength (supporting information Figure S9), we do not interpret the anisotropy magnitude but focus on fast directions. The largest errors are associated with nodes located at the margin of the study area as well as with nodes with very small magnitude of the anisotropy (supporting information Figure S10).

The lack of crossing paths caused by insufficient azimuthal coverage may lead to trade off between lateral heterogeneities and azimuthal anisotropy [*Lévêque et al.*, 1998; *Maggi et al.*, 2006]. To ameliorate this trade-

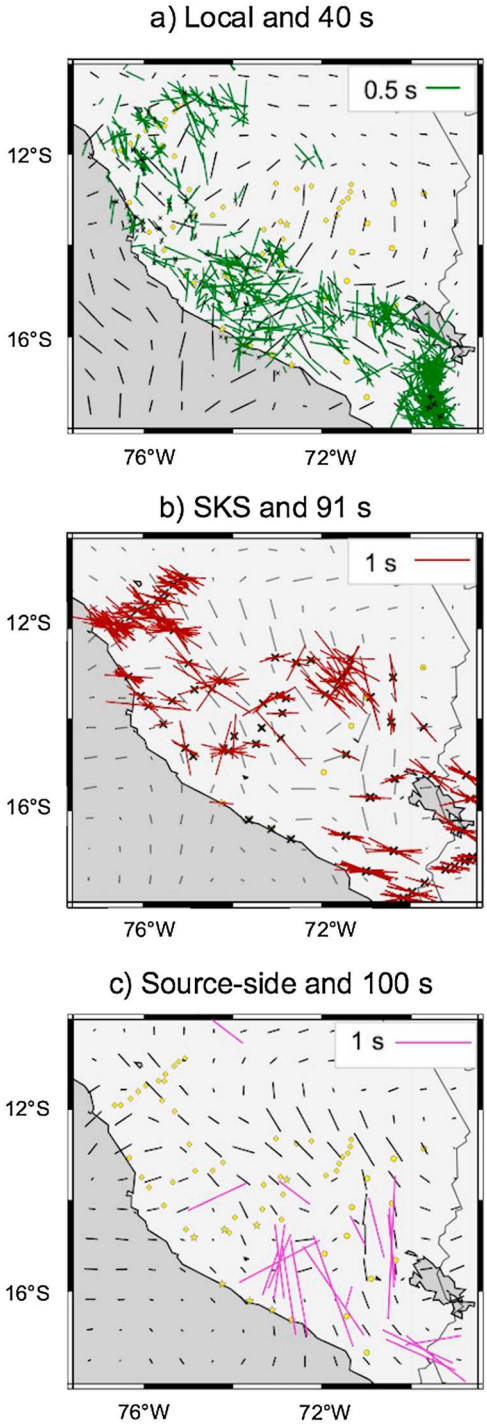

Figure 8. Comparison between shear wave splitting and Rayleigh wave azimuthal anisotropy. Shear wave splitting measurements are from *Eakin et al.* [2014], *Eakin et al.* [2015], *Eakin et al.* [2016], and *Long et al.* [2016]. (a) Local shear wave splitting (green bars) and 40 s. The measurements are plotted at the event location. (b) SKS splitting (red bars) and 91 s. (c) Source-side splitting (pink bars) and 100 s. Black crosses in Figures 8a and 8b are null measurements. Yellow circles are stations used in the study.

off we equalized and improved the back-azimuthal coverage by limiting events from oversampled back azimuths and adding smaller but well recorded events (see section 2). The comparison between isotropic and anisotropic phase velocity images (supporting information Figure S11) shows that allowing for azimuthal anisotropy has very small effects on resulting velocities and demonstrates that the resulting anisotropy does not trade off with isotropic phase velocity heterogeneities.

6. Discussion

6.1. Comparison Between Shear Wave Splitting and Rayleigh Wave Phase Anisotropy

The model for upper mantle anisotropy obtained in this study provides constraints complementary to those provided by shear wave splitting, which has previously been studied in this region by *Eakin et al.* [2014, 2015, 2016] and *Long et al.* [2016]. Here we briefly discuss the comparison between the two types of studies, illustrated in Figure 8. Figure 8a shows local shear wave splitting measurements from *Eakin et al.* [2014] and *Long et al.* [2016], plotted at the event location; event depths ranged from ~90 to ~130 km. For comparison, we overlaid our anisotropic phase velocity map at 40 s period, with peak sensitivity at ~50 km depth (Figure 2). Figure 8b shows SKS splitting measurements from *Eakin et al.* [2015] and *Long et al.* [2016], along with our 91 s period map, with peak sensitivity at ~140 km depth (Figure 2). Source-side measurements from *Eakin et al.* [2016], which mainly reflect anisotropy in the slab and subslab mantle, are shown in Figure 8c, along with the 100 s phase velocity map; peak sensitivity at this period is ~145 km.

We focus our comparison on the region where Rayleigh wave phase anisotropy is well resolved (Figure 7). Local S splitting measurements show very complex patterns across southern Peru (Figure 8a). Under the volcanic arc to the south the fast directions are predominantly trench parallel, consistent with our observations at short periods (brown dashed area in Figures 4a and 4b).

Another anisotropic pattern that can be observed with local S splitting measurements to the south, but inboard from the volcanic arc, is the roughly N-S alignment of fast directions (e.g., at ~15.5°S, ~71°W), consistent with the N-S alignment of fast directions at intermediate periods (45 s and 50 s) in our model. Based on peak sensitivity of these periods (Figure 2), the anisotropic layer may be constrained to depths between ~50 and ~70 km.

Along the southern edge of the flat slab, the local S splitting measurements show various alignments of fast directions, ranging from trench perpendicular to trench parallel. The trench-perpendicular alignment of fast directions can also be observed at short periods (33 s and 40 s) in our surface wave model. Since our short periods are sensitive to shallower structures, with peak sensitivities at ~40–~ 50 km depth (Figure 2), this suggests a contribution from anisotropy within the upper plate. The trench-parallel fast directions observed in local S splits are consistent with our observations at intermediate periods (red dashed area in Figures 4c–4e) with peak sensitivities between ~85 and 120 km depth, suggesting an anisotropic region within the slab itself. At long periods (91 s and 100 s) the fast directions along the southern edge of the flat slab are oriented N-S, parallel to slab contours at greater depths (Figure 1). The SKS and source-side splitting measurements also reveal dominant N-S striking fast directions here, consistent with our observations. This pattern has been attributed to the contorted subducting plate, which alters its fabric upon subduction due to extension in this corner [*Eakin et al*., 2016]. Our results are in agreement with this hypothesis. We further discuss this slab-related anisotropy in the following section. Two source-side splitting measurements show trench-subperpendicular fast directions in the flat slab region (at 73°W, ~15.5°S, ~14°S, ~74.5°W). Since we do not observe a similar pattern at our long periods, it is plausible that these fast directions illuminate anisotropic structures at greater depths, to which our long period measurements are no longer sensitive.

To the north, complex patterns observed with local and SKS splitting illuminate multilayered anisotropy [*Eakin and Long*, 2013; *Eakin et al*., 2015]. The SKS splitting measurements show fast directions ranging from trench parallel to trench perpendicular. The trench-parallel fast directions start to appear at ~14.5°S and continue farther north. This pattern can also be observed at long periods (Figure 4f and supporting information Figure S6c, brown dashed area), where it aligns with slow anomalies in our tomography. The SKS splitting measurements indicate roughly trench-perpendicular alignment of fast directions in the forearc and under the Western Cordillera. We also observe this anisotropic pattern at intermediate and long periods (Figures 4c–4f, green dashed area), where the pattern aligns with fast anomalies.

6.2. Trench-Parallel Anisotropy Beneath the Active Volcanic Arc

The along strike variations in slab geometry in southern Peru are accompanied by substantial changes in observed anisotropy. At the southern end of our study area where the Nazca plate subducts at a normal dip angle, we observe a trench-parallel alignment of fast directions at short periods (40–50 s, dashed orange area in Figures 4a and 4b and supporting information Figure S6b). The appearance of the trench-parallel anisotropy at shorter periods constrains the anisotropic layer to lie either within or above the slab. Trench-parallel alignment of fast directions in the mantle wedge above the subducting slab has been observed or inferred in other subduction zones, including in Costa Rica and Nicaragua [*Hoernle et al*., 2008], the Aleutians [*Mehl et al*., 2003], the Mariana subduction system [*Pozgay et al*., 2007], and in the Japanese Ryukyu arc [*Long and van der Hilst*, 2006]. These observations can be reconciled with viscous coupling between the downgoing plate and the overlying mantle wedge material, causing two-dimensional corner flow in the mantle wedge [e.g., *Fischer et al*., 2000], if the presence of B-type olivine fabric is invoked. B-type fabric tends to align fast axes perpendicular to the flow direction [*Jung and Karato*, 2001] and requires the presence of low temperatures, high stresses, and some amount of water [*Kneller et al*., 2005]. The seismicity along the steeply dipping slab in southern Peru is abundant [e.g., *Kumar et al*., 2016], suggesting the release of fluids into the wedge via metamorphic dehydration reactions [e.g., *Kirby et al*., 1996]. However, high heat flow [*Hamza et al*., 2005] and the presence of an active volcanic arc above the steeply dipping slab suggest elevated temperature and low stresses and thus conditions less favorable for the occurrence of B-type olivine.

Another possibility is arc parallel flow in the mantle wedge that can be caused by some combination of trench retreat and variations in slab dip [*Hoernle et al*., 2008; *Kneller and van Keken*, 2008]. According to this scenario the A-, C-, D-, or E- type olivine crystals tend to align the fast symmetry axis (*a* axis) in the warm mantle wedge roughly parallel to the flow. The ambient conditions in the mantle wedge beneath the active volcanic arc with elevated temperatures and high water content are favorable for the occurrence of C-type

olivine [*Karato et al*., 2008], which would be the best candidate to explain the observed pattern. This scenario would be consistent with trench-parallel flow in the back-arc mantle wedge further to the south recently inferred from the local splitting [*Long et al*., 2016].

A third possibility involves serpentine deformation within the hydrated mantle wedge [*Katayama et al*., 2009]. The serpentine tends to align the slow *c* axis orthogonally to the shear plane during the deformation. As mentioned earlier, the abundant seismicity might indicate dehydration of the slab and hydration of the mantle wedge. In addition, the low shear velocities we observe in this study above the steeply descending plate and beneath the active volcanic arc (Figure 3, transect CC′) likely relate to combination of high temperatures and presence of fluids.

A fourth possibility relates to fault-induced seismic anisotropy along the trench-parallel trending outer rise faults created by bending of the slab before entering the trench [*Faccenda et al*., 2008]. In this case the anisotropy is caused by crystallographic and shape-preferred orientation of hydrated fault surfaces [*Faccenda et al*., 2008] possibly in combination with dehydration and increased pore pressure in these fault zones during subduction [*Healy et al*., 2009]. Substantial shear wave velocity reduction along the upper part of the subducting plate and/or along the interface between two plates in southern Peru has been recently imaged by *Kim and Clayton* [2015]. The velocity reduction was interpreted as slab hydration of outer rise faults and subsequent dehydration upon subduction, consistent with this and previous scenarios. It is hard to discriminate between the last three scenarios, particularly since the sensitivity of surface waves at the relevant periods do not allow us to distinguish between anisotropy within the wedge and the shallow part of the subducting slab.

6.3. Evidence for Flow Through the Slab Tear

The slab geometry north of the subducting Nazca Ridge is very complex: the slab is torn to the west, while the flat slab remnants still persist to the east (Figure 3d) [*Antonijevic et al*., 2015]. The slab tear probably continues up to ~350 km depth [*Scire et al*., 2016].

One possible explanation for the trench-parallel fast directions that are aligned with the trench-parallel low-velocity anomaly north of the Nazca Ridge is that this low-velocity material represents asthenosphere flowing through the inferred tear in the Nazca Plate (Figure 9, anomaly "MF"). By comparing fast directions of long and intermediate periods we notice gradual westward progression of the trench-parallel pattern as the periods get shorter (Figures 9d, 9c, 9b, and 9a). This might suggest that the subslab mantle flow gets shallower from east to west, consistent with the asthenosphere flowing above the normally dipping slab to the west (anomaly "S" in Figure 9) and below the flat slab remnants to the east (anomaly "FSR" in Figures 9a and 9b). The direction of this flow is not well constrained. It could either be flowing from the mantle wedge above the normally dipping slab west of the tear to the subslab mantle beneath the flat slab or the other way around.

6.4. Low-Velocity Anomaly Beneath the Easternmost Corner of the Flat Slab

Probably the most striking feature we observe south of the inferred tear is a pervasive low-velocity anomaly at subslab depths beneath the inboard easternmost corner of the flat slab. As described earlier, instead of slab-related high velocities, we observe modest low velocities all along the plate below the subducted Nazca Ridge that becomes even further reduced ~250 km away from the trench (Figures 3c and 3e and supporting information Figure S5). The decrease in oceanic mantle-related fast velocities from west to east is also consistent with a recent receiver function study for events coming from the SE [*Ma and Clayton*, 2015].

Several factors could cause the absence of slab-related high velocities along the ridge upon subduction. First, we lose resolution west of our stations between the trench and the horizontal portion of the slab. This is because of a lack of stations offshore and because stations along the coast are usually noisier, meaning fewer useable data were obtained from these locations. Therefore, at least for areas west of our array, the lack of high velocities could simply be an artifact of undersampling. Second, the crust of the subducting Nazca Ridge is very thick (~18 km) [*Hampel et al*., 2004] and possibly hydrated [*Kim and Clayton*, 2015]. The hydrated, overthickened crust and upper sedimentary layers will have low shear wave velocities, which could vertically smear into the oceanic mantle lithosphere in our model, making the expected oceanic-lithosphere-related high velocities more difficult to resolve. Third, inherited mantle structures from the formation of the Nazca Ridge may result in persistent lower velocities in the associated mantle lithosphere. In general,

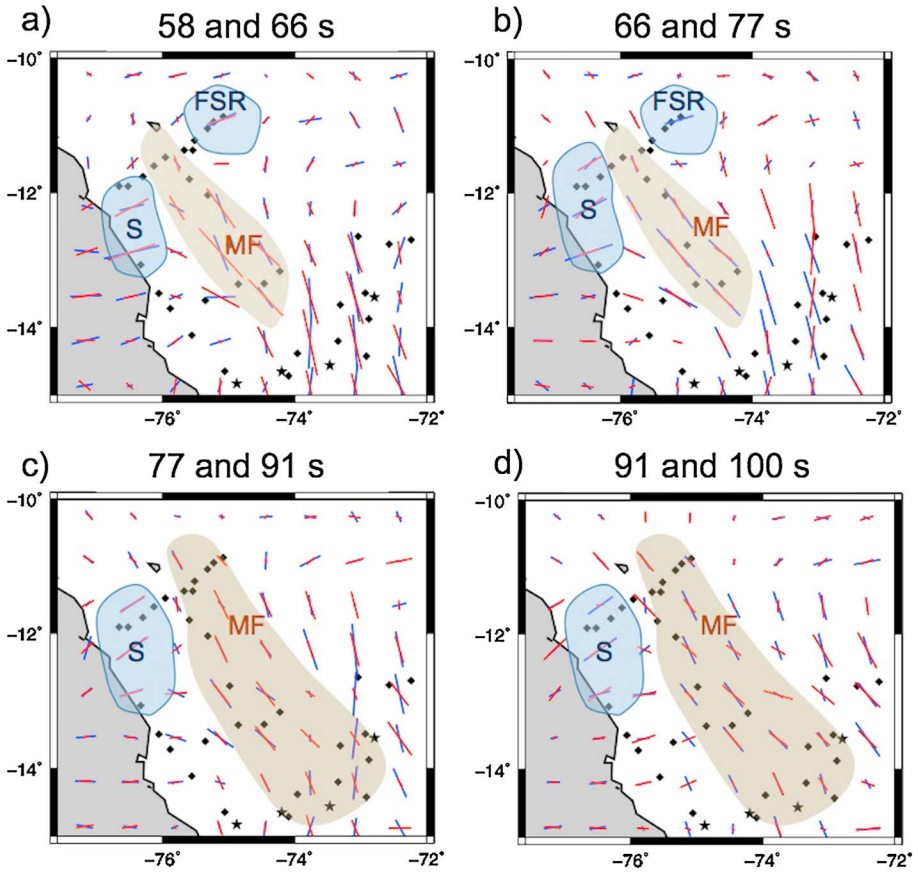

Figure 9. Inferred mantle flow through the slab tear. Bars are fast directions scaled according to magnitude. Black rectangles, circles, and stars are stations used in the study. (a) Overlaid fast directions for 58 s (blue bars) and 66 s (red bars). Inferred features: S = torn slab; MF = mantle flow; and FSR = flat slab remnant. (b) Overlaid fast directions for 66 s (blue bars) and 77 s (red bars). (c) Overlaid fast directions for 77 s (blue bars) and 91 s (red bars). (d) Overlaid fast direction for 91 s (blue bars) and 100 s (red bars).

asthenospheric flow in the form of small-scale convection and/or viscous fingering instabilities have been invoked to explain the formation of intraplate ridges and seamounts [*Weeraratne et al.*, 2007] and accompanied delayed cooling/thickening of the oceanic lithosphere [*Davaille and Lees*, 2004]. Recently, *Forsyth and Weeraratne* [2014] found high attenuation and low shear wave velocities beneath the Shatsky Rise in the northwestern Pacific. This area has not been affected by volcanism within the past ~150 Ma, which suggests that low-velocity anomalies beneath intraplate volcanic features can persist for long periods of time. *Woods and Okal* [1994] estimated a substantial reduction in shear wave velocity (below 4 km/s) under the Nazca Ridge in the eastern Pacific Ocean basin using Rayleigh waveforms that propagate along the entire length of the ridge. This velocity reduction may indicate the presence of small melt pockets beneath the ridge to the west. In addition, among samples of volcanic rocks obtained from the Nazca Ridge, a few were approximately 5–13 Ma younger than other samples, showing evidence of a rejuvenation of Nazca Ridge volcanism [*Ray et al.*, 2012]. The velocities we observe along the first ~250 km of subducted ridge are not exceptionally low (Figure 3e). This indicates either that partial melt does not exist beneath the ridge any longer or that partial melt regions are very small and localized. Furthermore, the intraplate volcanism could have delayed the usual cooling and thickening of oceanic lithosphere or even thermally ablated the existing mantle lithosphere. Thinned oceanic mantle lithosphere along the ridge in combination with vertically smeared low velocities from overthickened crust and limited resolution along the coastal region could produce the observed modest lower slab-related shear wave velocities at the first ~250 km of subducted ridge.

While inherited structures and resolution can provide an explanation for the moderately low velocities observed to the west, they do not explain the sharp decrease in velocity observed beneath the easternmost

corner of the flat slab. The anomaly is within the seismic array and is well resolved (Figure 5). Any inherited structure that might be invoked to explain velocities farther to the west would likely remain constant along the extent of the subducted Nazca Ridge. The abrupt additional decrease in velocities beneath the slab in this region requires additional explanation.

Several factors could contribute to the strengthening of the low-velocity anomaly beneath the easternmost corner of the flat slab. These include increases in temperature, the presence of volatiles, and the presence of partial melting. We can calculate only minimum amounts of change based on the observed decrease in velocity due to our likely underestimation of the actual low-velocity anomalies caused by damping of the inversion (see forward modeling in Figure 6 and supporting information Figure S12). In the absence of melting or volatiles, the difference in shear velocities from west to east would require an additional increase in temperature of at least ~200°C [*Cammarano et al*., 2003]. The presence of water would also reduce velocities, even in the absence of partial melting or temperature change. The effect of high water content is similar to that of increased temperature, with 0.15 wt % of water in olivine roughly corresponding to an increase in temperature for 200°C [*Karato*, 2003]. A combination of temperature and/or volatiles could promote melting which in turn would also have a pronounced effect on seismic velocities [*Katz et al*., 2003]. To recover the observed velocities, the presence of at least 1% partial melting (7.9% velocity deviation) [*Hammond and Humphreys*, 2000] over a 70–90 km thick vertical column or 2% partial melting (22% velocity deviation) within a 25–35 km thick vertical column is required (see forward modeling in supporting information Figure S12).

There are a number of possible scenarios that could lead to some combination of changes in temperature, volatiles, or partial melting beneath the easternmost corner of the flat slab. One possibility is delamination of the oceanic plate. However, we observe fast velocities above the proposed slab location, which suggests thermal shielding, consistent with a flat slab below it. The fast velocities above the flat slab have been observed in other recent studies [*Ma and Clayton*, 2014, 2015]. If the slab had delaminated, we would expect pervasive slow velocities. The feature is also unlikely to be caused by an inherited structure, since in that case the anomaly would be visible along the entire ridge track, both to the west and east. Thus, some degree of mantle flow under the easternmost corner of the flat slab must be involved in its formation. Roughly speaking, the subslab mantle in this region could flow trench parallel (either south to north or north to south), vertically, or both. Depending on the flow directions, different combinations of temperature, melting, and volatile presence emerge as contributing factors to this low-velocity anomaly.

In the absence of any vertical motion, mantle flow directed south to north (as suggested previously by *Russo and Silver* [1994]) should not produce radically different velocities along strike and is therefore difficult to reconcile with our observations. Vertical (upward directed) mantle flow, however, could explain our observations by introducing warmer material to the area directly beneath the inboard corner of the flat slab. A vertical component to mantle flow would be consistent with the observed nulls from SKS, sSKS, and PKS shear wave splitting beneath this portion of the flat slab [*Eakin et al*., 2015]. The low-velocity anomaly is reduced laterally with depth and confined to the inboard easternmost corner beneath the flat slab (Figure 3 and supporting information Figure S4). This suggests that any vertical flow and possible associated decompression partial melting is localized both laterally and in depth. Future examination of radial anisotropy (Rayleigh versus Love waves) is necessary to confirm the presence of such vertical flow.

Another possibility is the presence of water and possible associated flux melting. Normally, regional subslab low velocities are not attributed to increases in volatiles due to the absence of an obvious source of significant amounts of water. However, the inferred tear in the subducted plate to the north [*Antonijevic et al*., 2015] offers this additional intriguing possibility. If flow beneath this portion of the Nazca plate trends trench parallel from north to south instead south to north, the mantle from above the torn slab could be hydrated by that slab and then flow south, ending up below the flat slab. In this case, the observed trench-parallel alignment of fast directions north of the projected Nazca Ridge would correspond to the N-S directed flow. Eventually, this hydrated material might collect in the inboard corner of the contorted underside of the flat slab resulting in volatile-rich subslab mantle and/or flux melting (Figure 10). Given that the tear occurred recently [*Antonijevic et al*., 2015], this scenario is possible only if the volatile-rich subslab mantle had enough time to reach the edge of the flat slab region.

Both an increase in temperature/decompression melting and the presence of volatiles/flux melting can equally well explain the velocity reduction beneath the easternmost corner of the flat slab, so discriminating

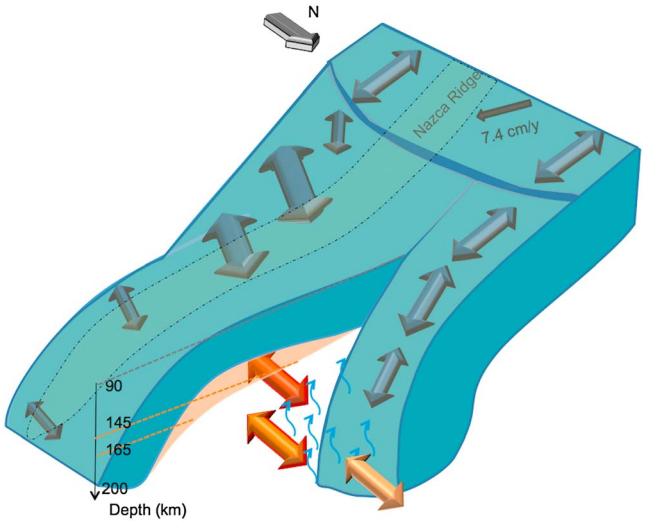

Figure 10. Schematic representation of the slab fabric and mantle flow through the tear. The top of the slab is inferred from earthquake distribution [*Antonijevic et al*., 2015]; lateral and vertical extent of the low-velocity anomaly is inferred from our 3-D shear wave velocity model. The black arrow denotes relative motion of the Nazca Plate [*Gripp and Gordon*, 2002]. Greenish area shows subducting Nazca Ridge. Blue arrows refer to slab fabric. Red arrows refer to mantle flow through the tear north of the ridge. If the mantle flows from south to north, it may carry hydrous phases released from the torn slab.

between the two is difficult. In either case, however, the observed anomaly might have important geodynamic implications since the material beneath this corner is presumably more buoyant than the surrounding mantle and/or could thermally ablate the slab from beneath. Recent high-resolution imaging of the southernmost part of the flat slab reveals an inboard upward motion of the flat slab roughly beneath the Western/Eastern Cordillera boundary [*Ma and Clayton*, 2015]. This unusual slab geometry has been attributed to interplate suction. However, the location of the flat slab's inferred upward deflection spatially coincides with this prominent low-velocity anomaly beneath the slab. The thermally ablated/thinned oceanic mantle lithosphere of the subducting ridge and/or presence of volatiles/partial melting below this corner could contribute to overall slab buoyancy, providing additional support to this upward motion. Future geodynamical modeling is necessary to better understand the effects of this anomaly to complex slab geometry in this corner.

6.5. Slab-Related Anisotropy

Some of our observed anisotropy is associated with the fast velocity anomalies of the subducted Nazca Plate. Before being subducted, oceanic plates usually preserve primary (fossilized) fabric dating from early slab formation along the mid-oceanic ridge. The direction of azimuthal anisotropy in young oceanic plates is typically related to A-type olivine within the oceanic lithospheric mantle, which tends to align fast axes along the spreading direction [e.g., *Hess*, 1964]. Even though this fossil fabric has been generally more successfully observed in the oceanic lithospheric mantle of younger oceanic plates, recent studies show that it can persist in older slabs, too. For example, using Rayleigh wave phase anisotropy, *Smith et al*. [2004] found evidence of stratification in azimuthal anisotropy with depth across the Pacific. They found that the fast directions in the upper lithosphere ($<$100 km) correlate well with paleospreading directions, reflecting fossilized azimuthal anisotropy, while greater depths illuminate current ambient flow direction. This primary (fossilized) fabric can persist upon entering the subduction zone [*Audet*, 2013] or can be modified upon subduction. The serpentinization along the outer-rise faults in the upper part of the slab [*Faccenda et al*., 2008] or, alternatively, substantial deformation within the slab due to rapid change in slab geometry [*Eakin et al*., 2016] can lead to alteration of the slab's primary fabric.

Recently, *Eakin et al*. [2016] demonstrated that the fossil slab fabric in the 200–400 km depth range in southern Peru is overprinted due to the substantial along strike extension that the slab undergoes while changing its geometry from flat to steep. According to their model, the CPO of olivine in this specific area rotates to become subparallel to the slab depth contours during deformation. Our observations along the southern margin of the flat slab are consistent with this model and extend that interpretation to shallower depths. We observe a rotation of fast axes from trench perpendicular to N-S/NNW-SSE at intermediate periods (58 s and 66 s) that correspond to the depth of the subducting plate (Figures 1 and 2). This anisotropic pattern is also aligned with fast velocities (dashed blue area in Figures 4c–4e) consistent with our interpretation of slab-related anisotropy. We observe the strongest anisotropy along the southern edge of the flat slab, where the slab is heavily contorted due to a rapid change in slab geometry from flat to steep [*Ma and Clayton*, 2014;

Phillips et al., 2012]. The orientation of fast axes along the southernmost edge of the flat slab/transition zone at intermediate periods (58 s and 66 s, Figures 4c and 4d) is consistent with the orientation of *T* axes (the maximum extension direction) inferred from focal mechanism solutions [*Kumar et al.*, 2016]. The pattern shifts inland at longer periods and aligns with slab contours (Figures 4e and 4f and supporting information Figures S6c and S6d), consistent with source-side splitting measurements [*Eakin et al.*, 2016] (Figure 8c). This suggests that modified slab fabric persists at greater depths.

Our observations are consistent with *Eakin et al.* [2016] along the southern margin of the flat slab. In areas north of the ridge, where the slab is torn and has resumed normal subduction [*Antonijevic et al.*, 2015], we find different patterns of slab-related anisotropy. We observe roughly trench-perpendicular fast directions at intermediate and longer periods aligned with a seismically fast anomaly (dashed green area in Figures 4c–4f), which we interpret as the anisotropic pattern coming from the slab west of the tear. This slab is not affected by flat slab-related deformation and therefore preserves its paleofabric. The contrast in the observed anisotropic patterns to the south and north illuminates differences in strain that the Nazca plate undergoes along the strike. We suggest that extension within the contorted slab to the south has led to alternation of the preexisting slab fabric, while the preservation of the fossil slab fabric to the north indicates that the slab here has not undergone the same deformation (Figure 10). This is additional evidence showing that the previously assumed extensive Peruvian flat slab is not uniformly flat along strike.

7. Conclusion

Observations of anisotropic Rayleigh wave phase velocities indicate that the complex slab geometry in southern Peru affects the surrounding mantle flow field. To the south, where the slab subducts steeply, we find trench-parallel oriented fast directions beneath the active volcanic arc that may relate either to the mantle wedge and/or subducting plate. To the north, beneath the easternmost corner of the flat slab, we find a pronounced low-velocity anomaly. The anomaly may be produced either by increased temperature and/or decompression melting due to small-scale vertical flow beneath this corner or by the presence of volatiles and/or flux melting that could be caused by southward directed, volatile-rich subslab mantle flow. Future examination of radial anisotropy should be able to verify the existence of vertical flow beneath this corner. In either case, the subslab material beneath this corner is presumably more buoyant than the surrounding mantle and may provide an additional dynamic contribution to the inferred upward deflection of the flat slab in this region.

Our results indicate that the mantle flow above the torn slab north of the subducted Nazca Ridge continues beneath the flat slab segment. We find that the tear created a new pathway that connects two mantle reservoirs. However, we are not able to determine whether the flow is directed N-S or S-N, since azimuthal anisotropy can reveal the orientation, but not the direction of mantle flow.

Based on slab-related anisotropy we find that the slab's internal deformation substantially varies along strike. South of the subducting Nazca Ridge the extension within excessively contorted slab alters the slab fabric. Our results indicate that this altered slab fabric persists at greater depths. In contrast, the slab tear to the north reduces the strain within the torn slab allowing the slab's primary (fossilized) fabrics to stay preserved upon subduction.

Acknowledgments

We are thankful to Donald Forsyth for access to his inversion codes. Collection of the PULSE and CAUGHT data sets was facilitated by the Incorporated Research Institutions for Seismology (IRIS). Data collected are available through the IRIS Data Management Center. We thank Robert Clayton and Paul Davies for providing the records from eight PERUSE stations. We acknowledge helpful comments from anonymous reviewers for suggestions that greatly improved the manuscript. The PULSE experiment was supported by NSF grants EAR-0944184 (LSW), EAR-0943991 (SLB), and EAR-0943962 (MDL). The CAUGHT project was supported by NSF grants EAR-0908777 (LSW) and EAR-0907880 (SLB).

References

Anderson, M. L., G. Zandt, E. Triep, M. Fouch, and S. Beck (2004), Anisotropy and mantle flow in the Chile-Argentina subduction zone from shear wave splitting analysis, *Geophys. Res. Lett.*, *31*, L23608, doi:10.1029/2004GL020906.

Antonijevic, S. K., L. S. Wagner, A. Kumar, S. L. Beck, M. D. Long, G. Zandt, H. Tavera, and C. Condori (2015), The role of ridges in the formation and longevity of flat slabs, *Nature*, *524*(7564), 212–215, doi:10.1038/nature14648.

Audet, P. (2013), Seismic anisotropy of subducting oceanic uppermost mantle from fossil spreading, *Geophys. Res. Lett.*, *40*, 173–177, doi:10.1029/2012GL054328.

Cahill, T., and B. L. Isacks (1992), Seismicity and shape of the subducted Nazca plate, *J. Geophys. Res.*, *97*(B12), 17,503–17,529, doi:10.1029/92JB00493.

Cammarano, F., S. Goes, P. Vacher, and D. Giardini (2003), Inferring upper-mantle temperatures from seismic velocities, *Phys. Earth Planet. Inter.*, *138*(3), 197–222, doi:10.1016/S0031-9201(03)00156-0.

Couch, R., and R. M. Whitsett (1981), Structure of the Nazca Ridge and the continental shelf and slope of southern Peru, *Geol. Soc. Am. Mem.*, *154*, 569–586, doi:10.1130/MEM154-p569.

Davaille, A., and J. M. Lees (2004), Thermal modeling of subducted plates: Tear and hotspot at the Kamchatka corner, *Earth Planet. Sci. Lett.*, *226*(3), 293–304, doi:10.1016/j.epsl.2004.07.024.

DeMets, C., R. G. Gordon, and D. F. Argus (2010), Geologically current plate motions, *Geophys. J. Int.*, *181*(1), 1–80, doi:10.1111/j.1365-246X.2009.04491.x.
Di Leo, J. F., A. M. Walker, Z. H. Li, J. Wookey, N. M. Ribe, J. M. Kendall, and A. Tommasi (2014), Development of texture and seismic anisotropy during the onset of subduction, *Geochem. Geophys. Geosyst.*, *15*, 192–212, doi:10.1002/2013GC005032.
Dougherty, S. L., and R. W. Clayton (2014), Seismic structure in southern Peru: Evidence for a smooth contortion between flat and normal subduction of the Nazca Plate, *Geophys. J. Int.*, *200*(1), 534–555, doi:10.1093/gji/ggu415.
Eakin, C. M., and M. D. Long (2013), Complex anisotropy beneath the Peruvian flat slab from frequency-dependent, multiple-phase shear wave splitting analysis, *J. Geophys. Res. Solid Earth*, *118*, 4794–4813, doi:10.1002/jgrb.50349.
Eakin, C. M., M. D. Long, S. L. Beck, L. S. Wagner, H. Tavera, and C. Condori (2014), Response of the mantle to flat slab evolution: Insights from local S splitting beneath Peru, *Geophys. Res. Lettt.*, *41*, 3438–3446, doi:10.1002/2014GL059943.
Eakin, C. M., M. D. Long, S. L. Beck, L. S. Wagner, H. Tavera, and C. Condori (2015), Upper mantle anisotropy beneath Peru from SKS splitting: Constraints on flat slab dynamics and interaction with the Nazca Ridge, *Earth Planet. Sci. Lett.*, *412*, 152–162, doi:10.1016/j.epsl.2014.12.015.
Eakin, C. M., M. D. Long, A. Scire, S. L. Beck, L. S. Wagner, G. Zandt, and H. Tavera (2016), Internal deformation of the subducted Nazca slab inferred from seismic anisotropy, *Nat. Geosci.*, *9*(1), 56–59, doi:10.1038/ngeo2592.
Faccenda, M., and F. A. Capitanio (2013), Seismic anisotropy around subduction zones: Insights from three-dimensional modeling of upper mantle deformation and SKS splitting calculations, *Geochem. Geophys. Geosyst.*, *14*, 243–262, doi:10.1002/ggge.20055.
Faccenda, M., L. Burlini, T. V. Gerya, and D. Mainprice (2008), Fault-induced anisotropy by hydration in subducting oceanic plates, *Nature*, *455*, 1097–1101, doi:10.1038/nature07376.
Fischer, K. M., E. M. Parmentier, A. R. Stine, and E. R. Wolf (2000), Modeling anisotropy and plate-driven flow in the Tonga subduction zone back arc, *J. Geophys. Res.*, *105*, 16,181–16,191, doi:10.1029/1999JB900441.
Forsyth, D. W., and A. Li (2005), Array analysis of two-dimensional variations in surface wave phase velocity and azimuthal anisotropy in the presence of multipathing interference, in *Seismic Earth: Array Analysis of Broadband Seismograms*, edited by A. Levander and G. Nolet, pp. 81–97, AGU, Washington D. C., doi:10.1029/157GM06.
Forsyth, D. W., and D. Weeraratne (2014), Attenuation in the Upper Mantle beneath "Normal" Old Seafloor in the Western Pacific DI44A-06, *AGU Fall Meeting 2014*, San Francisco, Calif.
Gripp, A. E., and R. G. Gordon (2002), Young tracks of hotspots and current plate velocities, *Geophys. J. Int.*, *150*(2), 321–361, doi:10.1046/j.1365-246X.2002.01627.x.
Gutscher, M. A., W. Spakman, H. Bijwaard, and E. R. Engdahl (2000), Geodynamics of flat subduction: Seismicity and tomographic constraints from the Andean margin, *Tectonics*, *19*(5), 814–833, doi:10.1029/1999TC001152.
Hammond, W. C., and E. D. Humphreys (2000), Upper mantle seismic wave velocity: Effects of realistic partial melt geometries, *J. Geophys. Res.*, *105*(10), 10,975–10,986, doi:10.1029/2000JB900041.
Hampel, A. (2002), The migration history of the Nazca Ridge along the Peruvian active margin: A re-evaluation, *Earth Planet. Sci. Lett.*, *203*(2), 665–679, doi:10.1016/S0012-821X(02)00859-2.
Hampel, A., N. Kukowski, J. Bialas, C. Huebscher, and R. Heinbockel (2004), Ridge subduction at an erosive margin: The collision zone of the Nazca Ridge in southern Peru, *J. Geophys. Res.*, *109*, B02101, doi:10.1029/2003JB002593.
Hamza, V. M., F. J. S. Dias, A. J. Gomes, and Z. G. D. Terceros (2005), Numerical and functional representations of regional heat flow in South America, *Phys. Earth Planet. Inter.*, *152*(4), 223–256, doi:10.1016/j.pepi.2005.04.009.
Healy, D., S. M. Reddy, N. E. Timms, E. M. Gray, and A. V. Brovarone (2009), Trench-parallel fast axes of seismic anisotropy due to fluid-filled cracks in subducting slabs, *Earth Planet. Sci. Lett.*, *283*(1), 75–86, doi:10.1016/j.epsl.2009.03.037.
Hess, H. H. (1964), Seismic anisotropy of the uppermost mantle under oceans, *Nature*, *203*, 629–631, doi:10.1038/203629a0.
Hoernle, K., et al. (2008), Arc-parallel flow in the mantle wedge beneath Costa Rica and Nicaragua, *Nature*, *451*(7182), 1094–1097, doi:10.1038/nature06550.
Jaillard, E., G. Hérail, T. Monfret, E. Díaz-Martínez, P. Baby, A. Lavenu, and J. F. Dumont (2000), Tectonic evolution of the Andes of Ecuador, Peru, Bolivia and northernmost Chile, *Tectonic Evol. South Am.*, *31*, 481–559.
James, D. E. (1971), Andean crustal and upper mantle structure, *J. Geophys. Res.*, *76*(14), 3246–3271, doi:10.1029/JB076i014p03246.
Jung, H., and S. I. Karato (2001), Water-induced fabric transitions in olivine, *Science*, *293*, 1460–1463, doi:10.1126/science.1062235.
Karato, S. I. (2003), Mapping water content in upper mantle, *AGU Geophys. Monogr. Ser.*, *138*, 135–152, doi:10.1029/138GM08.
Karato, S. I., H. Jung, I. Katayama, and P. Skemer (2008), Geodynamic significance of seismic anisotropy of the upper mantle: New insights from laboratory studies, *Ann. Rev. Earth Planet. Sci.*, *36*, 59–95, doi:10.1146/annurev.earth.36.031207.124120.
Katayama, I., K. I. Hirauchi, K. Michibayashi, and J. I. Ando (2009), Trench-parallel anisotropy produced by serpentine deformation in the hydrated mantle wedge, *Nature*, *461*(7267), 1114–1117, doi:10.1038/nature08513.
Katz, R. F., M. Spiegelman, and C. H. Langmuir (2003), A new parameterization of hydrous mantle melting, *Geochem. Geophys. Geosyst.*, *4*(9), 1073, doi:10.1029/2002GC000433
Kennett, B. L. N., and E. R. Engdahl (1991), Travel times for global earthquake location and phase identification, *Geophys. J. Int.*, *105*, 429–465, doi:10.1111/j.1365-246X.1991.tb06724.x.
Kim, Y., and R. W. Clayton (2015), Seismic properties of the Nazca oceanic crust in southern Peruvian subduction system, *Earth Planet. Sci. Lett.*, *429*, 110–121, doi:10.1016/j.epsl.2015.07.055.
Kirby, S., E. R. Engdahl, and R. Denlinger (1996), Intermediate-depth intraslab earthquakes and arc volcanism as physical expressions of crustal and uppermost mantle metamorphism in subducting slabs, *Subduction Top Bottom*, 195–214, doi:10.1029/GM096p0195.
Kneller, E. A., and P. E. Van Keken (2008), Effect of three-dimensional slab geometry on deformation in the mantle wedge: Implications for shear wave anisotropy, *Geochem. Geophys. Geosyst.*, *9*, Q01003, doi:10.1029/2007GC001677.
Kneller, E. A., P. E. van Keken, S. I. Karato, and J. Park (2005), B-type olivine fabric in the mantle wedge: Insights from high-resolution non-Newtonian subduction zone models, *Earth Planet. Sci. Lett.*, *237*, 781–797, doi:10.1029/2001DC000256.
Kumar, A., L. S. Wagner, S. L. Beck, M. D. Long, G. Zandt, B. Young, H. Tavera, and E. Minaya (2016), Seismicity and state of stress in the central and southern Peruvian flat slab, *Earth Planet. Sci. Lett.*, *441*, 71–80, doi:10.1016/j.epsl.2016.02.023.
Lévěque, J. J., E. Debayle, and V. Maupin (1998), Anisotropy in the Indian Ocean upper mantle from Rayleigh-and Love-waveform inversion, *Geophys. J. Int.*, *133*(3), 529–540, doi:10.1046/j.1365-246X.1998.00504.x.
Long, M. D., and R. D. van der Hilst (2006), Shear wave splitting from local events beneath the Ryukyu arc: Trench-parallel anisotropy in the mantle wedge, *Phys. Earth Planet. Inter.*, *155*(3), 300–312, doi:10.1016/j.pepi.2006.01.003.
Long, M. D., and T. W. Becker (2010), Mantle dynamics and seismic anisotropy, *Earth Planet. Sci. Lett.*, *297*(3), 341–354, doi:10.1016/j.epsl.2010.06.036.

Long, M. D., C. B. Biryol, C. M. Eakin, S. L. Beck, L. S. Wagner, G. Zandt, E. Minaya, and H. Tavera (2016), Overriding plate, mantle wedge, slab, and sub-slab contributions to seismic anisotropy beneath the northern Central Andean Plateau, *Geochem. Geophys. Geosyst.*, doi:10.1029/2016GC006316, in press.

Ma, Y., and R. W. Clayton (2014), The crust and uppermost mantle structure of Southern Peru from ambient noise and earthquake surface wave analysis, *Earth Planet. Sci. Lett.*, *395*, 61–70.

Ma, Y., and R. W. Clayton (2015), Flat slab deformation caused by interplate suction force, *Geophys. Res. Lett.*, *42*, 7064–7072, doi:10.1002/2015GL065195.

Macharé, J., and L. Ortlieb (1992), Plio-Quaternary vertical motions and the subduction of the Nazca Ridge, central coast of Peru, *Tectonophysics*, *205*(1), 97–108, doi:10.1016/0040-1951(92)90420-B.

Maggi, A., E. Debayle, K. Priestley, and G. Barruol (2006), Azimuthal anisotropy of the Pacific region, *Earth Planet. Sci. Lett.*, *250*(1), 53–71, doi:10.1016/j.epsl.2006.07.010.

Mehl, L., B. R. Hacker, G. Hirth, and P. B. Kelemen (2003), Arc-parallel flow within the mantle wedge: Evidence from the accreted Talkeetna arc, south central Alaska, *J. Geophys. Res.*, *108*(B8), 2375, doi:10.1029/2002JB002233

Müller, R. D., M. Sdrolias, C. Gaina, and W. R. Roest (2008), Age, spreading rates, and spreading asymmetry of the world's ocean crust, *Geochem. Geophys. Geosyst.*, *9*, Q04006, doi:10.1029/2007GC001743.

Peyton, V., V. Levin, J. Park, M. Brandon, J. Lees, E. Gordeev, and A. Ozerov (2001), Mantle flow at a slab edge: Seismic anisotropy in the Kamchatka region, *Geophys. Res. Lett*, *28*(2), 379–382, doi:10.1029/2000GL012200.

Phillips, K., and R. W. Clayton (2014), Structure of the subduction transition region from seismic array data in southern Peru, *Geophys. J. Int.*, *504*, doi:10.1029/2012JB009540.

Phillips, K., R. W. Clayton, P. Davis, H. Tavera, R. Guy, S. Skinner, and V. Aguilar (2012), Structure of the subduction system in southern Peru from seismic array data, *J. Geophys. Res.*, *117*, B11306, doi:10.1029/2012JB009540.

Porritt, R. W., T. W. Becker, and G. Monsalve (2014), Seismic anisotropy and slab dynamics from SKS splitting recorded in Colombia, *Geophys. Res. Lett.*, *41*, 8775–8783, doi:10.1002/2014GL061958.

Pozgay, S. H., D. A. Wiens, J. A. Conder, H. Shiobara, and H. Sugioka (2007), Complex mantle flow in the Mariana subduction system: Evidence from shear wave splitting, *Geophys. J. Int.*, *170*(1), 371–386, doi:10.1111/j.1365-246X.2007.03433.x.

Ray, J. S., J. J. Mahoney, R. A. Duncan, J. Ray, P. Wessel, and D. F. Naar (2012), Chronology and geochemistry of lavas from the Nazca Ridge and Easter Seamount Chain: An ~ 30 Myr hotspot record, *J. Petrol.*, *53*, 1417–1448, doi:10.1093/petrology/egs021.

Rosenbaum, G., D. Giles, M. Saxon, P. G. Betts, R. F. Weinberg, and C. Duboz (2005), Subduction of the Nazca Ridge and the Inca Plateau: Insights into the formation of ore deposits in Peru, *Earth Planet. Sci. Lett.*, *239*(1), 18–32, doi:10.1016/j.epsl.2005.08.003.

Russo, R. M., and P. G. Silver (1994), Trench-parallel flow beneath the Nazca plate from seismic anisotropy, *Science*, *263*(5150), 1105–1111, doi:10.1126/science.263.5150.110.

Saito, M. (1988), DISPER80: A subroutine package for calculation of seismic normal-mode solutions, in *Seismological Algorithms: Computational Methods and Computer Programs*, edited by D. J. Doornbos, pp. 293–319, Elsevier, New York.

Scire, A., G. Zandt, S. Beck, M. Long, L. Wagner, E. Minaya, and H. Tavera (2016), Imaging the transition from flat to normal subduction: Variations in the structure of the Nazca slab and upper mantle under southern Peru and northwestern Bolivia, *Geophys. J. Int.*, *204*(1), 457–479, doi:10.1093/gji/ggv452.

Skemer, P., and L. N. Hansen (2015), Inferring upper-mantle flow from seismic anisotropy: An experimental perspective, *Tectonophysics*, doi:10.1016/j.tecto.2015.12.003.

Skemer, P., J. M. Warren, and G. Hirth (2012), The influence of deformation history on the interpretation of seismic anisotropy, *Geochem. Geophys. Geosyst.*, *13*, Q03006, doi:10.1029/2011GC003988.

Smith, D. B., M. H. Ritzwoller, and N. M. Shapiro (2004), Stratification of anisotropy in the Pacific upper mantle, *J. Geophys. Res.*, *109*, B11309, doi:10.1029/2004JB003200.

Smith, M. L., and F. A. Dahlen (1973), The azimuthal dependence of Love and Rayleigh wave propagation in a slightly anisotropic medium, *J. Geophys. Res.*, *78*(17), 3321–3333, doi:10.1029/JB078i017p03321.

Snoke, J. A., I. S. Sacks, and D. E. James (1979), Subduction beneath western South America: Evidence from converted phases, *Geophys. J. R. Astronom. Soc.*, *59*(1), 219–225, doi:10.1111/j.1365-246X.1979.tb02562.x.

Steinberger, B. (2002), Motion of the Easter hot spot relative to Hawaii and Louisville hot spots, *Geochem. Geophys. Geosyst.*, *3*(11), 8503, doi:10.1029/2002GC000334

Tassara, A., H. J. Götze, S. Schmidt, and R. Hackney (2006), Three-dimensional density model of the Nazca plate and the Andean continental margin, *J. Geophys. Res.*, *111*, B09404, doi:10.1029/2005JB003976.

Uyeda, S., T. Watanabe, Y. Ozasayama, and K. Ibaragi (1980), Report of heat flow measurements in Peru and Ecuador, *Bull. Earthquake Res. Inst.*, *55*, 55–74.

Ward, K. M., R. C. Porter, G. Zandt, S. L. Beck, L. S. Wagner, E. Minaya, and H. Tavera (2013), Ambient noise tomography across the Central Andes, *Geophys. J. Int.*, *194*(3), 1559–1573, doi:10.1111/j.1365-246X.2011.05313.x.

Weeraratne, D. S., D. W. Forsyth, K. M. Fischer, and A. A. Nyblade (2003), Evidence for an upper mantle plume beneath the Tanzanian craton from Rayleigh wave tomography, *J. Geophys. Res.*, *108*(B9), 2427, doi:10.1029/2002JB002273.

Weeraratne, D. S., D. W. Forsyth, Y. Yang, and S. C. Webb (2007), Rayleigh wave tomography beneath intraplate volcanic ridges in the South Pacific, *J. Geophys. Res.*, *112*, B06303, doi:10.1029/2006JB004403.

Woods, M. T., and E. A. Okal (1994), The structure of the Nazca ridge and Sala y Gomez seamount chain from the dispersion of Rayleigh waves, *Geophys. J. Int.*, *117*(1), 205–222, doi:10.1111/j.1365-246X.1994.tb03313.x.

Yang, Y., and D. W. Forsyth (2006), Regional tomographic inversion of the amplitude and phase of Rayleigh waves with 2-D sensitivity kernels, *Geophys. J. Int.*, *166*(3), 1148–1160, doi:10.1111/j.1365-246X.2006.02972.x.